Phase diagram analysis of high-pressure/high-temperature polymorphs of ammonia borane

Satoshi Nakano,[1,*] *Hiroshi Fujihisa,*[2] *Hiroshi Yamawaki,*[2] *and Takumi Kikegawa*[3]

[1] National Institute for Materials Science (NIMS), Tsukuba, Ibaraki 305-0044, Japan

[2] National Metrology Institute of Japan (NMIJ), National Institute of Advanced Industrial Science and Technology (AIST), Tsukuba, Ibaraki 305-8565, Japan

[3] Photon Factory (PF), Institute of Materials Structure Science (IMSS), High Energy Accelerator Research Organization (KEK), Tsukuba, Ibaraki, 305-0801 Japan

KEYWORDS: Ammonia borane, high-pressure, high-temperature, transformation, crystal structure, dihydrogen bond

ABSTRACT

Ammonia borane (NH_3BH_3) is a promising hydrogen-storage material because of its high hydrogen density. It is employed as a hydrogen source when synthesizing superconducting polyhydrides under high pressure. Additionally, NH_3BH_3 is a crystallographically interesting compound that features protonic hydrogen ($H^{\delta+}$) and hydridic hydrogen ($H^{\delta-}$), and it forms a dihydrogen bond, which explains its stable existence as a solid. Herein, X-ray diffraction experiments were performed at high pressures (HPs) and high temperatures (HTs) of up to 30 GPa and 300°C, respectively, to investigate the HP/HT phase diagram of NH_3BH_3. A new HP/HT phase (HPHT2) was identified above 9 GPa and 150°C. Crystal-structure analysis using the Rietveld method and stability verification using density functional theory calculations revealed that HPHT2 has a $P2_1/n$ ($Z = 4$) structure, similar to that of a previously reported HP/HT phase (HPHT) that appears at a lower pressure. HPHT2 is denser than the HP phases that appear at room temperature (HP1 and HP2) at the same pressure (up to ~17 GPa). In the phase diagram, the phase-boundary line between HPHT and HP1 is a downward convex curve. These unconventional phenomena in the density and phase boundary can attributed to the influence of dihydrogen bonding on the crystal structure and phase diagram.

INTRODUCTION

Ammonia borane (NH_3BH_3) holds promise as a hydrogen-storage material because of its high hydrogen density (gravimetric hydrogen density = 19.6 wt% and volumetric hydrogen density = 145 gH/L), and many studies have explored its basic structural properties and applications.[1,2] Among hydrides, NH_3BH_3 is practical because of its stability against atmospheric humidity, attributed to the slightly polar nature of hydrogen atoms in the NH_3BH_3 molecule. In other words, the hydrogen bonded to nitrogen behaves as a slightly positively charged protonic hydrogen ($H^{\delta+}$), whereas the hydrogen bonded to boron behaves as a slightly negatively charged hydridic hydrogen ($H^{\delta-}$). Between adjacent NH_3BH_3 molecules, these charged hydrogens attract each other to form a stable dihydrogen bond.[3] This explains why NH_3BH_3 exists as a stable solid molecular crystal, whereas ethane (C_2H_6), which has the same electronic structure, exists as a gas under ambient conditions.

Hydrogen is chemically flexible and can behave as atomic hydrogen (protium, H_0), positively charged proton (H^+), negatively charged hydride (H^-), and covalently bonded hydrogen atoms (H_{cov}), which provide various physical/chemical properties in hydrides and hydrogen-containing compounds.[4] In such compounds, a dihydrogen bond is formed between the positively and negatively charged hydrogens. Therefore, studies on the role of dihydrogen bonds in the structures of materials can improve our understanding of the various structural properties attributed to hydrogen and provide valuable insights for designing hydrogen-containing materials with new functions. However, only few examples have been reported and the research on inorganic compounds is limited, whereas many studies have been conducted in the field of organic chemistry.[5] Therefore, further research on NH_3BH_3, which is a typical inorganic compound with dihydrogen bonds, is required.

Recently, polyhydrides such as LaH_{10}, which are synthesized under high-pressure (HP), have been attracting significant research interest because they exhibit superconductivity at a high critical temperature (*Tc*).[6,7] NH_3BH_3 has been employed as a hydrogen source in the synthesis of such polyhydrides because it releases hydrogen under HP/high-temperature (HT) conditions. However, the structural changes associated with the decomposition and hydrogen release behavior of NH_3BH_3 under HP/HT have not been investigated in detail.

Under ambient pressure, NH_3BH_3 does not have a HT phase because the ambient phase (AP, α-NH_3BH_3, phase I: *I*4*mm* structure) decomposes at approximately 110°C, accompanied by the release of hydrogen.[8] The decomposition and release of hydrogen proceed in multiple stages, and finally yielding hBN at 1500°C. The decomposition temperature of the AP increases with increasing pressure.[9,10] Conversely, regarding the structural change at room temperature (RT) and under HPs, the AP transforms into the first HP phase (HP1, β-NH_3BH_3, phase III: *Cmc*2_1 structure) at ~1.2 GPa and subsequently into the second HP phase (HP2, γ-NH_3BH_3, phase IV: *P*2_1 ($Z = 2$) structure) at ~11 GPa.[11] We investigated the relationship between the structures of these HP phases and the dihydrogen bond using HP X-ray diffraction (XRD), HP neutron diffraction, and HP Raman scattering.[12,13] In HP1, only half of the hydrogens formed dihydrogen bonds immediately after the transformation from the AP at 1.2 GPa. Additionally, under further compression at pressures above 4 GPa, all of the hydrogens formed dihydrogen bonds while maintaining the structure of *Cmc*2_1, and the bulk modulus increased. In HP2, all the hydrogen atoms formed dihydrogen bonds under stable pressure conditions (10–20 GPa).

Regarding the structural change of NH_3BH_3 under the HP/HT condition, Nylén et al. obtained a phase diagram at pressures and temperatures of up to 12 GPa and 300°C by HP Raman scattering and HP XRD, and they identified a HP/HT phase (HPHT, phase V: *Pnma* (Z =4)).[14,15] Wang et al.[16]

have investigated the structures of the HPHT and HP1 phases by *ab initio* molecular dynamics and proposed another more stable structure with the same symmetry as HPHT. In the proposed structure, the molecular position shifted, and the dihydrogen bonds of HPHT were weaker than those of HP1. In those reports, the structures of HPHT and HP1 were compared, however, there was no comparison with HP2. Chen et al.[17] and Lin et al.[18] reviewed the studies on the phase transition of NH_3BH_3 and summarized them in phase diagrams; however, the conditions were limited to pressures and temperatures below 10 GPa and room temperature, respectively. It is important to investigate structural polymorphs under expansive HP/HT conditions, and understanding the relationship between the structures and dihydrogen bonds is important for compensating for the few examples of inorganic compounds with dihydrogen bonds and for characterizing dihydrogen bonds. In addition, the expansion of the HP/HT conditions will improve our understanding of the decomposition of NH_3BH_3 and its hydrogen release behavior.

In this study, we performed XRD experiments at HPs and HTs of up to ~30 GPa and ~300°C, respectively, to discover new phases and investigate the HP/HT phase diagrams. In addition, we compared the structures of the phases and investigated the influence of dihydrogen bonds on the structures.

EXPERIMENTAL SECTION

Preparation of the sample and high-pressure cell

Commercially available NH_3BH_3 powder (purity > 97%, Sigma-Aldrich, USA) was ground in a SiO_2 glass mortar and used as a sample in the experiments. After grinding, the two-dimensional (2D) XRD analysis was implemented, and good ring patterns without broadening were observed.

A Mao-Bell-type diamond anvil cell (DAC) equipped with a pair of 1/4 Carat diamond anvils with a 600-μm-sized diameter cullet was used for the HP/HT XRD measurements. A rhenium sheet with thickness in the range of 250–300 μm was pre-indented between the anvils to a thickness of 50–70 μm for the gasket, and a hole with a 300-μm diameter was drilled in the center using an electric discharge machine. The sample powder and ruby balls (10–15 μm^{ϕ}), as pressure markers, were loaded into the sample chamber, which was assembled using the gasket and anvils. Most experiments were conducted without a pressure medium, and in some experiments, we used a He pressure medium (G1 grade, purity > 99.99995 vol.%), which was loaded onto the sample chamber using a gas-loading system.[19] Although no significant difference was observed in the phase-transition conditions of NH_3BH_3 between the presence and absence of the pressure medium, the broadening of the XRD pattern under HP was reduced, owing to the improvement in hydrostatisity when the He medium was used.

For the external heating of the DAC, a band heater (Sakaguchi Electric Heaters Co. Ltd., MIE13, 300 W) was placed over the cylinder of the Mao-Bell DAC. A sheathed K-type thermocouple for temperature control was interposed between the band heater and the DAC. The input power to the heater was controlled using a proportional-integral-differential controller with a temperature control unit (CHINO Co., SU12N1140-LANNNN). To protect the DAC and the stage on which it was placed, cooling water was circulated through the lever arm of the DAC. Figure S1 shows a schematic of the DAC configuration prepared as described above.

Temperature and pressure measurements

The temperature of the sample was measured using a ceramic-coated K-type thermocouple with a diameter of 0.2 mm^{ϕ} cemented to the slope of the anvil. As the diamond anvil exhibits high thermal conductivity, the sample temperature can be assumed to be approximately the same as the anvil temperature. The thermoelectromotive force of the thermocouple was measured using a digital recorder (Keyence Co., TR-W1050), and it was converted into temperature using the reference junction compensation function of the recorder (compensation accuracy = ±0.5°C) for zero-junction compensation. When a power of ~200 W was applied to the band heater, the heater temperature reached ~360°C and the sample temperature was ~300°C.

The pressure of the sample was determined from the shift in the fluorescence line (R1) of the ruby ball placed in the sample chamber. The fluorescence spectrum excited using a solid-state laser (488 nm, maximum 16 mW) was analyzed using a single monochromator (Spectral Products Co., Digikröm DK240, f = 0.24 m) with a 1200 g/mm grating and detected using a charge-coupled device detector (Apogee Instruments Inc., Alta U30-OE, 1024 × 256 array, 26 × 26 μm/px). The spectrograph was calibrated in terms of the wavelength using a Ne lamp with an accuracy of ±0.04 nm. The ruby fluorescence spectrum was measured, and the R1 line was fitted to a Gaussian function to obtain the peak wavelength. However, at a high temperature of ~300°C, the ruby fluorescence line became weak and broad, and the wavelength of the R1 line was read visually. Although the peak position of R1 is a function of both pressure and temperature, the pressure value can be calculated by assuming that the pressure and temperature independently shift the R1 line.[20] We calculated the standard wavelength (λ_{T0} (nm)) of the R1 line at ambient pressure from the sample temperature (T (K)) using Eq. (1),[21] after which we calculated the pressure with the observed wavelength (λ_T (nm)) and λ_{T0} (nm) using Eq. (2).[22] The pressure was calculated using Eq. (3) of the hydrostatic pressure equation[23] when the He medium was used. The pressure accuracy was estimated to be ±0.08 GPa at RT and approximately ±0.1 GPa at ~300 °C.

$$\lambda_{T0} = \frac{10^7}{14423 + 4.49\times10^{-2}T - 4.81\times10^{-4}T^2 + 3.71\times10^{-7}T^3}, \quad (1)$$

$$P_T = \frac{1904}{7.665}\left\{\left[1 + \frac{\lambda_T - \lambda_{T0}}{\lambda_{T0}}\right]^{7.665} - 1\right\}, \quad (2)$$

$$P_T = \frac{1904}{7.715}\left\{\left[1 + \frac{\lambda_T - \lambda_{T0}}{\lambda_{T0}}\right]^{7.715} - 1\right\}. \quad (3)$$

Generally, in HP experiments, the pressure accuracy may become a problem due to the pressure distribution within the sample chamber.[24] The pressure distribution was confirmed by placing some ruby balls in the sample chamber in the same experiments. When the pressure near the center of the sample chamber was ~20 GPa at RT, the maximum decrease in pressure was ~0.2 GPa at a position ~70 μm away from the center. As described later, the incident X-ray beam was collimated to 60–100 μm for the XRD measurements. The pressure accuracy was estimated within ~0.2 GPa for the XRD measurements because the pressure values were measured from a ruby placed within ~70 μm from the center of the sample chamber. Moreover, the pressure distribution inside the sample chamber decreased at HT. The reason why the pressure distribution was small even without using a pressure medium might be because the sample NH_3BH_3 was a very soft molecular crystal and Re, a very hard metal, was used for the gasket. In general, the pressure gradient is proportional to the yield strength. Therefore, when measuring a soft sample using a hard gasket, the pressure gradient in the sample chamber is much smaller than that in the gasket.

High-pressure/high-temperature X-ray diffraction measurements

HP/HT angle-dispersive XRD measurements were performed using synchrotron radiation at BL-18C of the Photon Factory (PF) at the High Energy Accelerator Research Organization (KEK).

The X-ray beam was monochromated at 20 keV and introduced into the sample in the DAC through a collimator with a pinhole having a diameter of 60–100 μm.

After changing either the pressure or temperature and waiting until the value stabilized during ~10–15 min, the XRD patterns were collected for 10–15 min. The temperature remained stable within ±1°C during the measurements. However, because the pressure may change slightly during the measurement (particularly at HTs), the pressure was measured immediately before and after the measurement, and the average value was obtained.

Diffraction patterns were collected using an image plate detector in the transmission geometry. The examples of the 2D diffraction patterns were shown in Figure S2. The 2D diffraction patterns were radially integrated into 1D profiles using the IPAnalyzer image analysis software.[25] Using PDindexer,[25] we analyzed the profiles and determined the phases of the samples, lattice parameters, and unit cell volumes.

An HP/HT phase diagram of NH_3BH_3 was drawn from the conditions and the identified phases. When a phase transition occurs, previous and new phases often co-exist. However, when a new phase peak appeared, the new phase was considered to be thermodynamically stable. The measurements were conducted via multiple routes under similar HP/HT conditions. Phase boundaries that could be objectively considered valid were drawn if there were variations in the results. Therefore, this phase diagram is strictly an experimental reaction diagram, but it can be regarded as an almost thermodynamic phase diagram.

Computational details of the structural analysis of a new phase

A material simulation and modeling software (BIOVIA Materials Studio (MS) Reflex; version 2022 HF1)[26] was used for the Rietveld analyses of the XRD data. The molecular shape of NH_3BH_3 was treated as a rigid body. The lattice parameters, three translational coordinates, and three rotational parameters of the molecule were refined with the March–Dollase preferred orientation correction.[27] To obtain accurate hydrogen positions, the atomic positions were optimized by fixing the cell parameters using the MS-CASTEP DFT software.[28] The GGA–PBEsol (Perdew–Burke–Ernzerhof for solids) exchange-correlation functionals[29] and the on-the-fly generated norm-conserving pseudopotentials[30] were employed. The cut-off energy for the plane-wave basis set was 990.0 eV. A $6 \times 4 \times 4$ Monkhorst–Pack grid[31] for the primitive cell was chosen for the k-point set, and k-separations of ~0.04 Å^{-1} were produced. The maximum force tolerance, maximum atomic displacement, and energy convergence tolerance were 0.001 eV/Å, 5.0×10^{-5} Å, and 5.0×10^{-7} eV/atom, respectively.

RESULTS AND DISCUSSION

Phase transitions and a new high-pressure/high-temperature phase

At 100°C and under ambient pressure, the shape of the NH_3BH_3 aggregates observed using optical microscopy and the XRD pattern of the AP did not change. When the temperature was increased to 120 °C, some substances adhered to the surface of the anvil and the XRD peaks disappeared, although the sample shape was maintained. At RT, the AP peaks did not recover. This indicated that NH_3BH_3 was decomposed or at least, the original crystal structure was broken, between 100°C and 120°C under ambient pressure.

The temperature dependence of the XRD pattern of NH_3BH_3 at ~4 GPa is shown in Figure 1. Under compression at 4.4 GPa and RT, the AP underwent a pressure-induced transformation into HP1. When the temperature was increased to 101°C, a phase transition to HPHT occurred, similar to the case reported in the previous.[15] At 180°C, the peak intensity weakened, and at 200°C, most of the peaks disappeared. This decomposition temperature was ~20°C lower than that reported by Nylén et al.[14] The decomposition temperature of NH_3BH_3 decreases with prolonged reaction time, even under ambient pressure,[32] and this difference of ~20°C might be attributed to the differences in the heating rate and duration.

Figure 2(a) shows the XRD patterns obtained in another measurement (Run #A). In this measurement, the AP was compressed up to ~8 GPa, and the temperature was increased to 200°C, thereafter, the pressure was increased with the temperature kept constant at 200°C. At 7.0 GPa and 200°C, a single phase of HPHT was observed. By increasing the pressure at the fixed temperature, a few small XRD peaks appeared at 9.1 GPa. As the pressure was further increased, the XRD pattern changed gradually up to 15.6 GPa, and above which no further change occurred. This XRD pattern did not indicate the HP phases (HP1, HP2, and HP3) observed at RT; rather it revealed a new HPHT phase (HPHT2) of NH_3BH_3. HPHT2 could be quenched at RT under HP by rapid cooling from 200°C. However, during decompression, multiple phase transitions occurred at pressures below 4 GPa and the phase finally returned to the AP, whereas HPHT2 could not be recovered under ambient conditions.

In another experiment (Run #B), HP2 was heated to 200°C at ~10 GPa, after which the pressure was released, as shown in Fig. 2(b). HP2 transformed into HPHT2 at 140°C during the heating process at ~10 GPa. Subsequently, in the decompression process at 200°C, HPHT2 transformed into HPHT at 7.7 GPa. Thus, at a constant temperature of 200°C, the phase transition from HPHT to HPHT2 started at ~9.1 GPa. Conversely, the phase transition from HPHT2 to HPHT occurred at ~8.8 GPa. That is, there was almost no hysteresis in the HPHT-HPHT2 phase transition at 200°C.

Crystal structure of the new high-pressure/high-temperature phase (HPHT2) and its relationship with the HPHT structure

The crystal structure of the newly discovered HP/HT phase, HPHT2, was analyzed using its XRD pattern. An initial structural model was searched by trusting the experimental diffraction intensity, and a structural model with a configuration similar to the *Pnma* structure of HPHT was obtained. However, the obtained atomic coordinates contain errors owing to the effects of the preferred orientation and nonuniform diffraction intensity. To alleviate the influence of these errors and obtain the coordinates of hydrogen, the coordinates of all atoms were optimized using DFT calculations.

Figure 3(a) and (b) show the results of the Rietveld analysis of the diffraction patterns obtained at 17.5 GPa and 200°C in Figure 2(a) and at 10.1 GPa and 200°C in Figure 2(b), respectively. These profiles could be explained with a structural model of the monoclinic $P2_1/n$ ($Z = 4$) space group shown in Figure 3(c), although the matching of the peak intensity ratios is poor. This is because the atomic coordinates of all atoms are fixed to the DFT-optimized positions. As mentioned later, this mismatch is thought to be due to the kinetic problem in the transformation to HPHT2 and the insufficient hydrostatic conditions. The refinement parameters, including the atomic positions of HPHT2 at 17.5 GPa and 200°C, which correspond to the information in Figure 3(a), are listed in Table 1.

Figure 4 shows the correspondence between the crystal structures of HPHT and HPHT2. They are similar, and the *ab*-, *bc*-, and *ca*-planes of HPHT2 correspond to the *ca*-, *ab*-, and *bc*-planes of HPHT, respectively. In HPHT, the NH_3BH_3 molecules are aligned along a plane perpendicular to the *b* axis, whereas in HPHT2 they are aligned at a slight angle from the corresponding plane perpendicular to the *c* axis. Consequently, the gaps between the NH_3BH_3 molecules in HPHT are filled to some extent in HPHT2.

Here, the hydrogen atoms bonding to the nitrogen and boron atoms are denoted as Hin and Hib, respectively, and three kinds of hydrogen atoms with different atomic positions are numbered as i = 1, 2, and 3, as described in the previous literature.[12] In HPHT2, all hydrogen atoms, written as Hin and Hib (i = 1–3), display different atomic positions (H1n, H2n, H3n, H1b, H2b, and H3b); therefore, there are nine types of hydrogen–hydrogen (H–H) distances between adjacent molecules. Contrarily, with respect to HPHT, only four types of H–H distances are established because the B–N axis of all molecules is parallel to the *ca*-plane, and Hin and Hib each have only two types of atomic positions (H1n, H2n, H1b, and H2b). The H–H distance in adjacent molecules in HPHT2 is shown in Table 2, compared with that in HPHT. In both HPHT2 and HPHT, all the H–H distances are closer than 2.4 Å, and therefore, every protonic hydrogen ($H^{\delta+}$) forms a dihydrogen bond with a hydridic hydrogen ($H^{\delta-}$) of the adjacent molecule. Regarding HPHT2, H1n–H3b and H3n–H1b at 10.1 GPa have two kinds of H–H distances, which are lower than 2.4 Å. This indicates that the dihydrogen bonds contributed by one hydrogen atom are formed not only between two adjacent molecules but also among three or more adjacent molecules. Moreover, when the pressure is increased to 17.5 GPa, additional dihydrogen bonds are formed also in H1n–H2b and H2n–H2b. Figure S3 displays the dihydrogen bonds that H1n forms with adjacent molecules in the crystal structure of HPHT2 at 17.5 GPa.

High-pressure/high-temperature phase diagram of NH_3BH_3

Similar HP/HT experiments were conducted via various P–T paths, and the phase relationships at pressures and temperatures up to 30 GPa and 300°C, respectively, were investigated. Figure 5 shows the HP/HT phase diagram obtained by accumulating these results. The phase-boundary lines of AP/HP1, HP1/HP2, and HP2/HP3 are almost perpendicular to the pressure axis of the phase diagram. However, it is thermodynamically inappropriate, essentially because it implies that "$dP/dT = 0$." This diagram is strictly an experimental reaction diagram; therefore, the results may be strongly influenced by a kinetic problem of the transformations near RT.

The new HP/HT phase, HPHT2, appeared at pressures above ~9 GPa and temperatures above 150°C –200°C. In the phase diagram, HPHT2 is adjacent to HP1, HP2, and HP3, in addition to HPHT, and any of these phases undergo a phase transformation into HPHT2 when the pressure or temperature changes. However, the transformation is sluggish, and the influence of the phase before the transition is remained in the XRD profiles. Therefore, there are often some differences in the peak intensity ratios that are attributed to the phase transition from a different phase to HPHT2. Additionally, the hydrostaticity of the sample might not be sufficient because most of the experiments were conducted without a pressure medium. These are the possible reasons why the HPHT2 profiles observed in Figures 2 and 3 appear to have different patterns even under similar conditions. However, all the peaks in the profiles, which were obtained by the structural analysis described above, could be assigned to HPHT2 and the phase before the transition.

In the P–T diagram in Figure 5, another new phase, i.e., HPHT3, can be observed above 230°C and 6–16 GPa. Under these conditions, some broad peaks were observed in the XRD profiles, which differed significantly from the patterns of other phases of NH_3BH_3. Figure 6(a) shows the XRD profiles of the formation of HPHT3 from HPHT2 during the decompression process from 14.7 to 9.7 GPa and 200°C to 251°C. The profile of HPHT3 is simple and seems easy to analyze. However, the visible peaks could not be explained by a simple cubic index, such as 111 or 200, and the structure of HPHT3 could not be analyzed. The HPHT3 phase was quenchable at RT, and it recovered under almost ambient pressure, as shown in Figure 6(b). Figure S4 displays an optical micrograph of the samples recovered from the experiment shown in Figure 6. A translucent but nonuniform texture may suggest a mixed state of HPHT3 and any other substances.

Although the details of the crystal structure of HPHT3 are not clear, the broad diffraction peaks and the simple pattern may suggest a major structural change, including partial decomposition. Liang et al.[33] investigated the decomposition reaction of NH_3BH_3 under high pressures using the first-principles molecular dynamics calculations. They predicted that H_2 is released by a decomposition reaction different from that occurring under ambient pressure. They reported that the NH_3BH_3 molecule itself separates two hydrogen atoms and releases H_2 at ambient pressure and high temperature. At 6 GPa, however, $H^{\delta+}$, which forms a dihydrogen bond with $H^{\delta-}$ of the adjacent molecules, is attracted by the dihydrogen bond and moves to the $H^{\delta-}$ side of the adjacent molecule to form $-BH_4$. Thereafter, then H_2 is released from $-BH_4$, and aminoborane (NH_2BH_2) remains. Considering their calculation results, the HPHT3 obtained in this study may be assigned to monomeric aminoborane (NH_2BH_2) or polyaminoborane ($(NH_2BH_2)_n$).

Liang et al. also suggested that different P–T paths lead to different structures and different phase diagrams.[33] In the present study, although the difference in the peak intensity ratio of HPHT2 was found to depend on the P–T path, there was almost no influence on the phase-boundary lines and the phase diagram.

Influence of dihydrogen bonds in high-pressure/high-temperature phase diagrams

As shown in the HP/HT phase diagram, the phase boundary between HP1 and HPHT shows a downward convex shape, indicating a point where dT/dP = 0, at 4 ~GPa. At 4 GPa, pressure-induced dihydrogen bonds were formed upon compression of HP1 at RT. Below ~4 GPa, only half of the hydrogens in HP1 form dihydrogen bonds with adjacent molecules; further compression reduces the intermolecular distances, and above ~4 GPa, all hydrogens in HP1 form dihydrogen bonds.[12] The pressure-induced formation of dihydrogen bonds also induces abnormal changes in the pressure dependence of the lattice parameters. The lattice parameter *a* of HP1 exhibits a downwardly convex pressure dependence for up to ~3 GPa, after which it monotonically decreases above ~3 GPa.[13] This strange pressure dependence of the lattice parameter was also reported by Liang et al. via first-principles calculations[33]; they attributed this phenomenon to the formation of dihydrogen bonds during compression.

As considered above, the unconventional shape of the HP1/HPHT phase boundary indicates that there are two regions with different numbers of dihydrogen bonds under the thermodynamically stable conditions of HP1. This virtual phase-boundary line is displayed with a dotted line in Figure 5. In other words, this boundary line confirms the pressure-induced formation of dihydrogen bond.

Pressure dependence of the volume of the new high-pressure/high-temperature phase (HPHT2)

To consider the influence of dihydrogen bonds on the polymorphic structure of NH_3BH_3 in detail, the pressure dependence of the molar volume of each phase was compared, as shown in Figure 7. Regarding the HP phases appearing at RT, the volumes at RT are displayed in the figure. For the HP/HT phases, we show the volumes at a temperature of 200°C obtained in the following experiments: HPHT→HPHT2 transformation by compression (Run #A) and HPHT2→HPHT transformation by decompression (Run #B).

The volume change associated with the HPHT→HPHT2 transformation at 200°C was –2.6% at ~14 GPa. It is reasonable that HPHT2 has a higher density than HPHT as HPHT2 appears at a higher pressure than HPHT. As described previously, the NH_3BH_3 molecules in HPHT2 are arranged to fill the intermolecular gap in HPHT. Conversely, comparing the volumes of the HP phases and the HP/HT phases, the volume of HPHT at 200°C and that of HP1 at RT are almost the same at the same pressure. In addition, the volume of HPHT2 at 200°C is smaller than that of HP2 at RT immediately after the HPHT→HPHT2 transformation. The volume difference between the two phases becomes less pronounced as the pressure increases, and the volumes are almost the same above ~17 GPa.

Generally, the HT phase is less dense than the RT phase at the same pressure. Regarding NH_3BH_3, however, HPHT at 200°C has almost the same density as HP1 at RT at the same pressure. Furthermore, HPHT2 at 200°C is denser than HP2 at RT up to 17 GPa. Such a strange phenomenon could be due to the influence of dihydrogen bonds. In HP2, $–NH^{\delta+}{}_3$ and $–BH^{\delta-}{}_3$ of the dumbbell-shaped NH_3BH_3 molecules form dihydrogen bonds, maintaining a gap between the molecules. The dihydrogen bonds combine $H^{\delta+}–N–B–H^{\delta-}$ and $H^{\delta-}–B–H^{\delta-}$ or $H^{\delta+}–N–H^{\delta+}$ of the molecules to construct four-membered and six-membered rings three-dimensionally and to form a cluster-like sparse structure (Figure S5). Conversely, the structure of HPHT2 might be relaxed by thermal vibration at a HT; when this occurs, the molecules become more parallel and fill the intermolecular gaps, resulting in a denser structure. This might be analogous to the role of hydrogen bonds in the ice crystal at ambient pressure, i.e., the ice crystal composed of hydrogen bonds undergoes melting to water with higher density when the temperature is elevated. Considering that the HP/HT phase at 200°C is denser than the HP phase at RT, their phase-boundary line should show a negative slope ($dT/dP < 0$) in the phase diagram, which contradicts Figure 5. Indeed, there are not enough measurement points to determine the phase-boundary line between HPHT2 and HP2; therefore, it is necessary to conduct further experiments and long-term measurements for more accurate information.

CONCLUSIONS

We conducted XRD experiments at HPs and HTs of up to 30 GPa and 300°C and investigated the HP/HT phase diagram of NH_3BH_3. The phase boundary between the first HP phase (HP1) and the HP/HT phase (HPHT) showed a downward convex shape, which could be attributed to the pressure-induced formation of dihydrogen bonds in HP1 at ~4 GPa. At 9 GPa and above 150°C, a new HP/HT phase (HPHT2) was identified, and it was determined to have a monoclinic $P2_1/n$ (Z= 4) crystal structure. The structure is similar to that of HPHT, but NH_3BH_3 molecules tilt to fill the gaps between the adjacent molecules. HPHT2 has a higher density than the HP phases (HP1 and HP2) that appear at RT and the same pressure, which could be due to the influence of dihydrogen bonds.

FIGURES

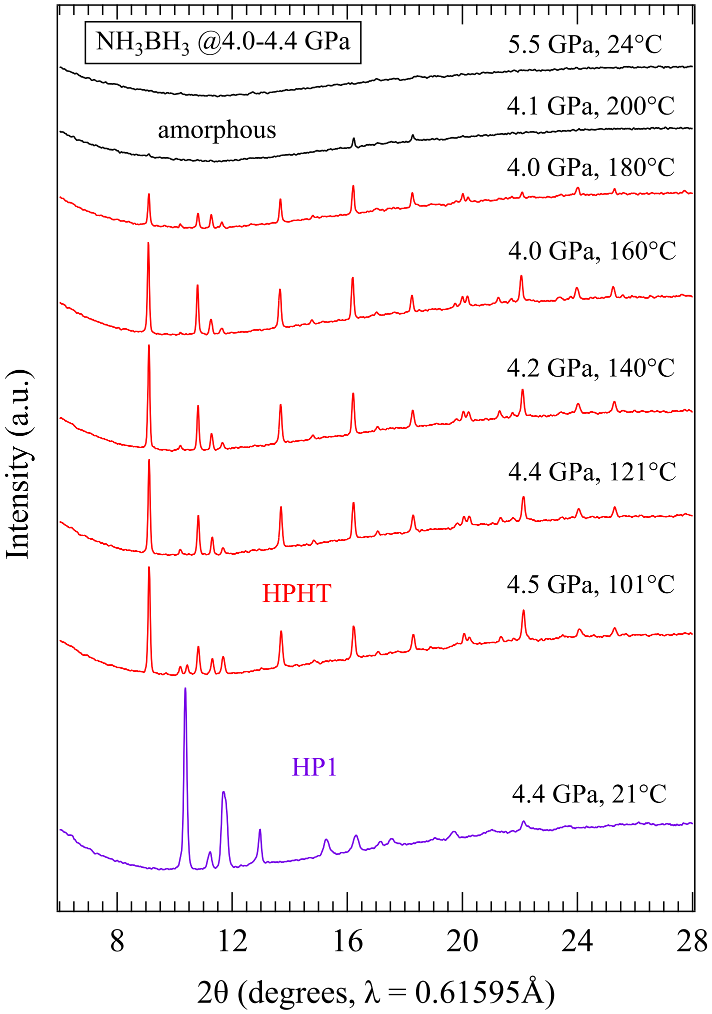

Figure 1. Change in the XRD patterns of NH_3BH_3 with increasing temperature at ~4 GPa. HP1 and HPHT denote the first high-pressure phase and the high-pressure/high-temperature phase, respectively.

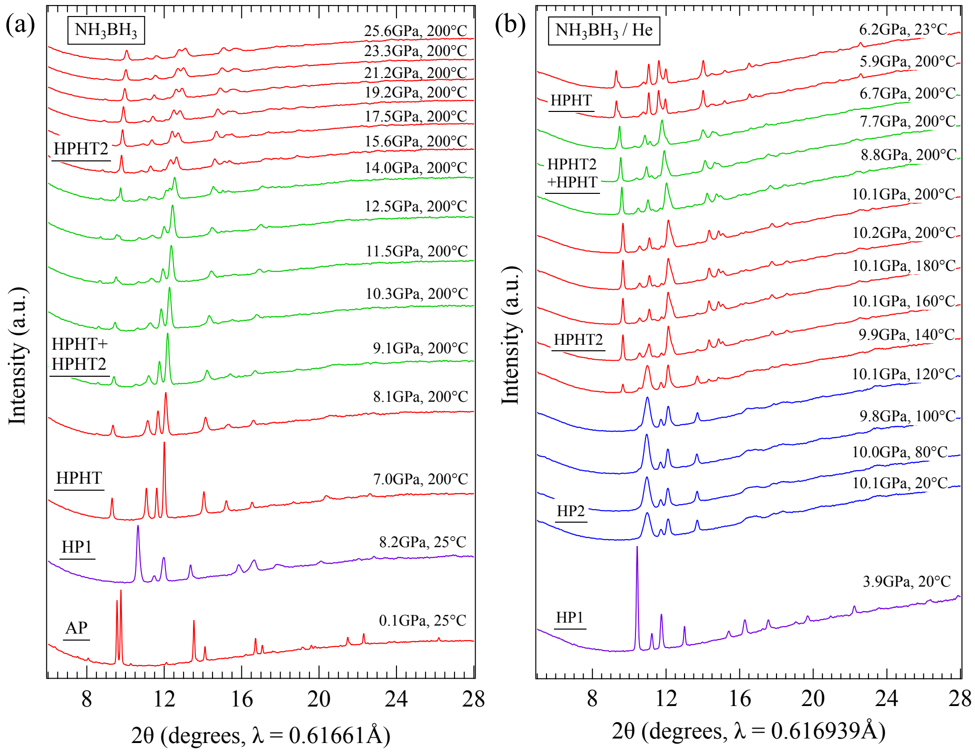

Figure 2. Change in the XRD patterns of NH_3BH_3 via various pressure–temperature paths. AP, HP1, HP2, HPHT and HPHT2 denote the ambient phase, the first high-pressure phase, the second high-pressure phase, the high-pressure/high-temperature phase, and the newly discovered high-pressure/high-temperature phase, respectively. In the measurement shown in (a) (Run #A), AP was compressed up to ~8 GPa, and the temperature was elevated to 200°C. Thereafter, the pressure was increased at a constant temperature of 200°C. In the measurement shown in (b) (Run #B), the AP transformed initially into HP1 and subsequently into HP2 during the compression at room temperature. After that, HP2 was heated to 200°C at ~10 GPa, after which the pressure was released.

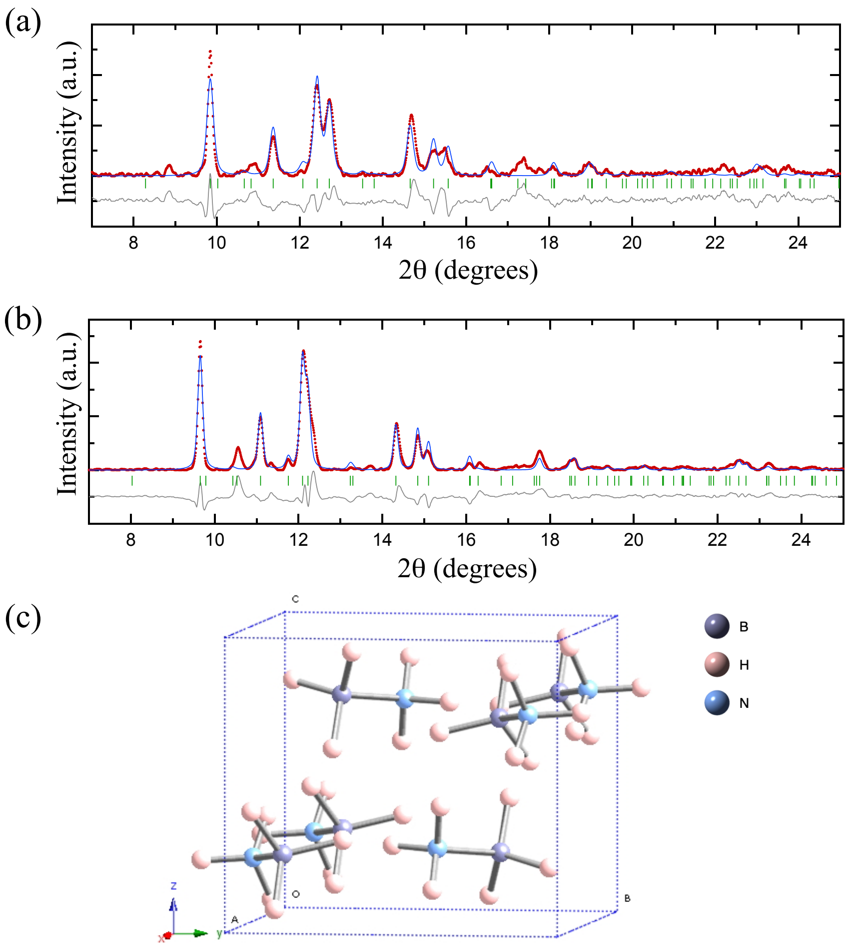

Figure 3. The results of the Rietveld analysis and the structural model of the newly discovered HPHT2 phase. (a) and (b) The results of the Rietveld analysis for the XRD patterns obtained at 17.5 GPa and 200°C and at 10.1 GPa and 200°C, respectively. The red dots and blue lines represent the observed and calculated intensities, respectively. The vertical green bars indicate the location of the calculated diffraction lines. The black line at the bottom indicates the difference between the observed and calculated intensities. The reliability factors of the fits are R_{wp} = 29.63 %, R_e = 22.30 %, S = 1.33 for (a) and R_{wp} = 22.24 %, R_e = 17.06 %, S = 1.30 for (b). The crystal structure of HPHT2 was analyzed with the monoclinic $P2_1/n$ ($Z = 4$) space group shown in Figure 3(c). The purple, blue, and red balls represent boron, nitrogen, and hydrogen atoms, respectively.

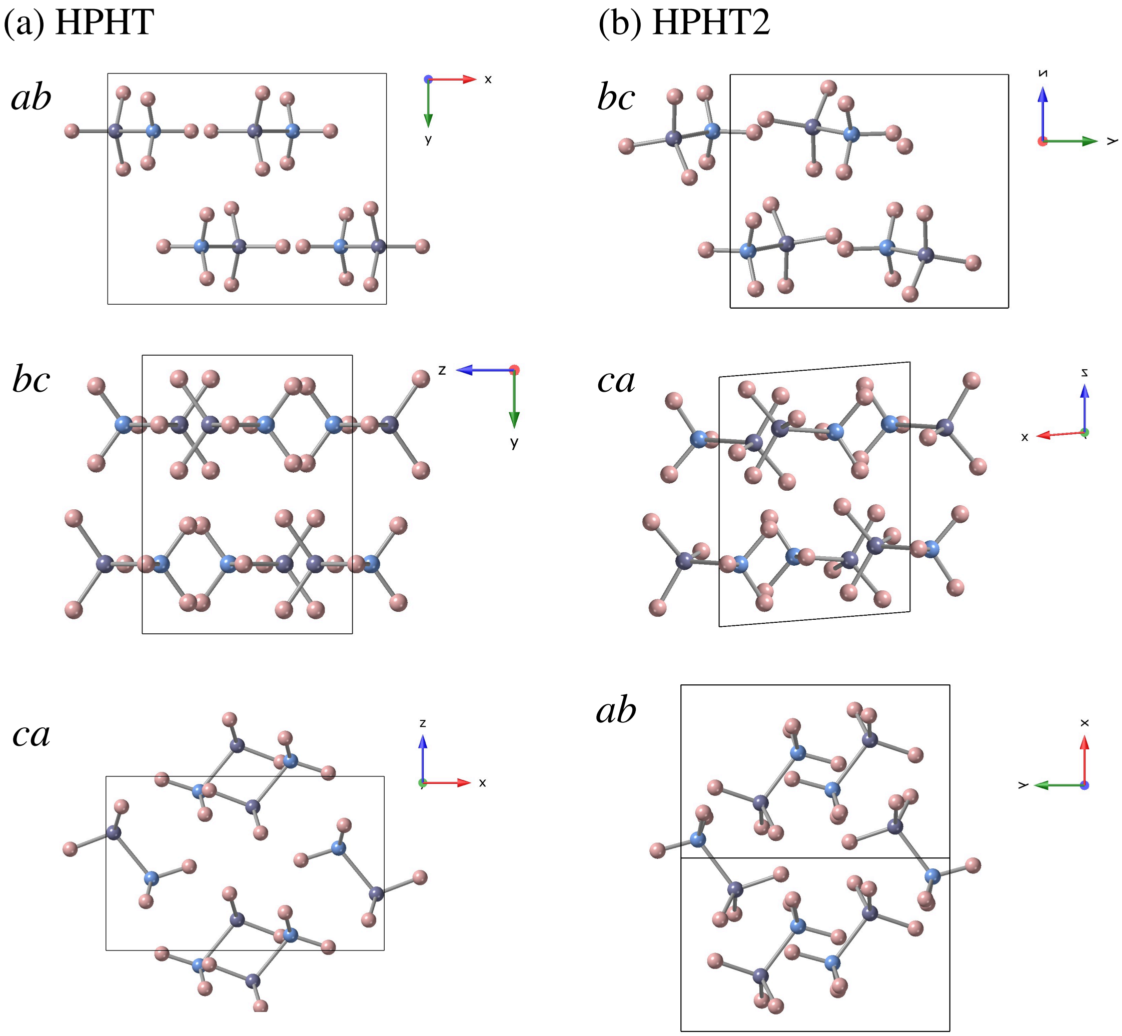

(a) HPHT

(b) HPHT2

Figure 4. Correspondence between the crystal structures of HPHT and HPHT2. The purple, blue, and red balls represent boron, nitrogen, and hydrogen atoms, respectively.

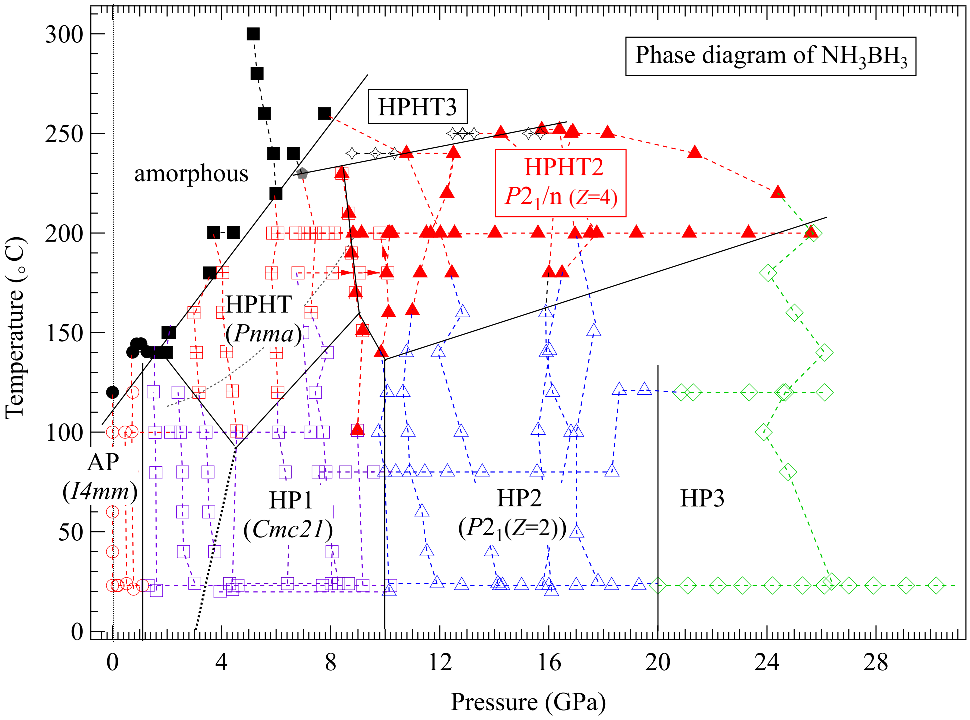

Figure 5. HP/HT phase diagram of NH_3BH_3 up to 30 GPa and 300°C. The solid line in the phase diagram represents the phase-boundary lines estimated from the XRD results. The dashed line in the HP1 region highlights the separation of regions with different numbers of dihydrogen bonds. The thin, dashed line in the HPHT region represents the phase boundary between HP1 and HPHT, as reported by Nylén et al.[15] HPHT2 is the newly discovered HP/HT phase in the present study. The HPHT3 was also observed, however, it might be a component produced by the decomposition of NH_3BH_3. The crystal structure of HP3 remains unknown.

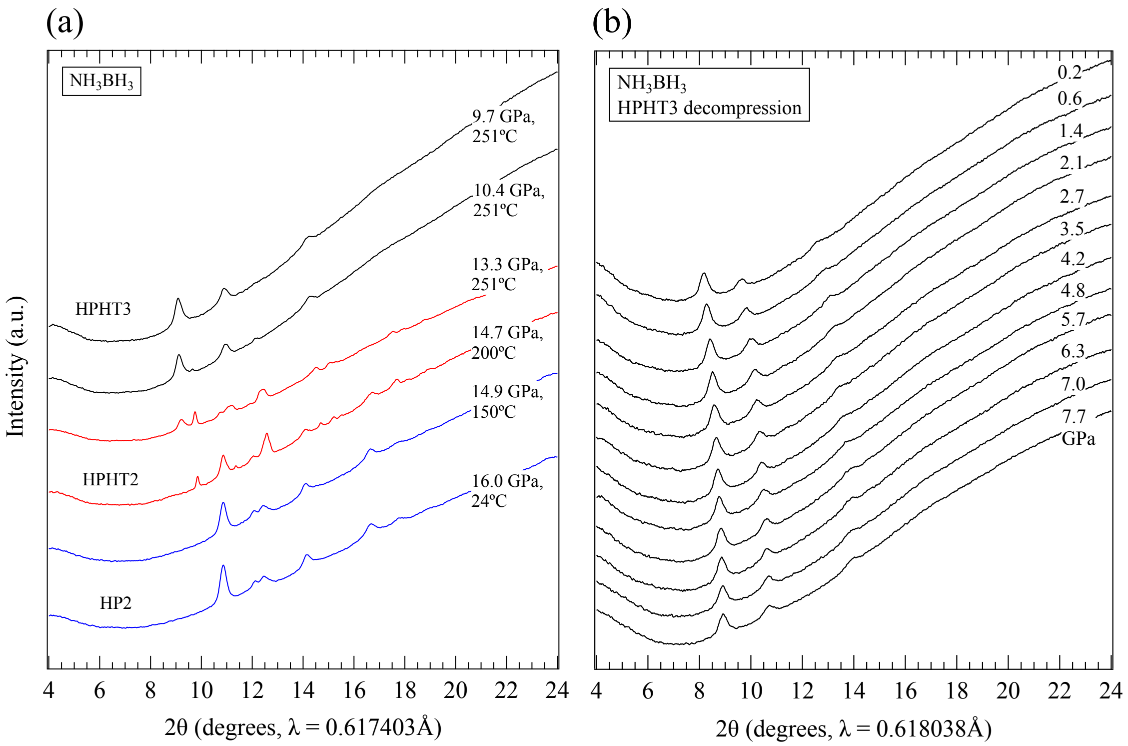

Figure 6. XRD patterns of (a) the formation of HPHT3 from HPHT2 and (b) the recovered HPHT3 after quenching at room pressure and the decompression.

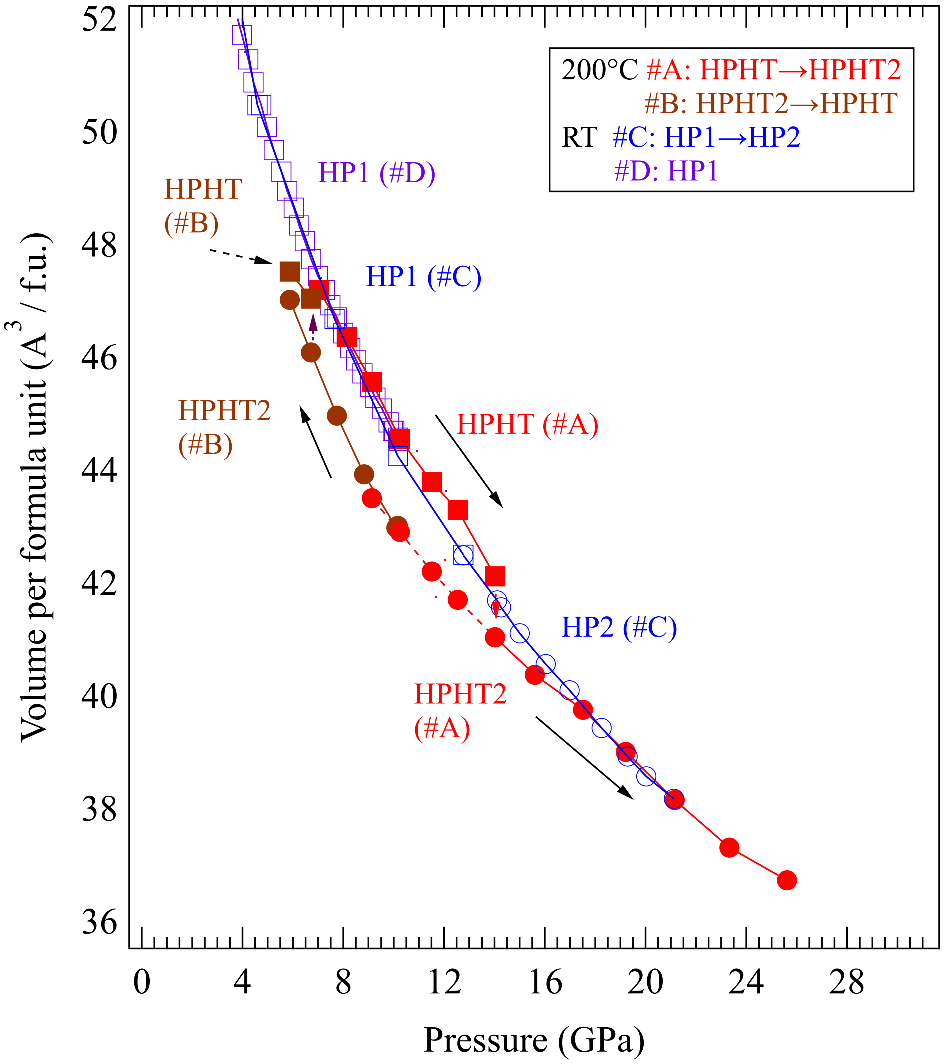

Figure 7. Pressure dependence of the molar volumes for the phases of NH_3BH_3. This figure shows four experimental results: (1) compression of HPHT and the transformation to HPHT2 at 200°C (Run #A, red); (2) decompression of HPHT2 and the transformation to HPHT at 200°C (Run #D, brown); (3) compression of HP1 and the transformation into HP2 at room temperature (Run #C, blue); and (4) compression of HP1 at room temperature (Run #D, purple). The open square, open circle, solid square and solid circle represent HP1, HP2, HPHT and HPHT2, respectively.

TABLES.

Table 1. Refinement parameters[a] of the new high-pressure/high-temperature phase (HPHT2) at 17.5 GPa and 200°C.

Space group: $P2_1/n$ ($Z = 4$)

$a = 4.2861$ Å, $b = 6.6360$ Å, $c = 5.5873$ Å, and $\beta = 94.5443°$

atom	*x*	*y*	*z*
N	-0.10679	0.06377	0.24306
B	0.18209	0.20317	0.27435
H1	-0.23699	0.09119	0.08135
H2	-0.04298	-0.08633	0.24815
H3	0.35515	0.14631	0.44137
H4	-0.26156	0.08386	0.37430
H5	0.32185	0.19899	0.09523
H6	0.09352	0.37247	0.30790

a) x, y, and z are the fractional position coordinates, and a, b, and c are the lattice parameters.

Table 2. List of the inter-hydrogen distances in adjacent molecules in HPHT2 and HPHT with distance closer than 2.4 Å.

Hxn–Hxb	HPHT2			
	10.1 GPa & 200 °C		17.5 GPa & 200 °C	
H1n–H1b	1.994		1.962	
H1n–H2b	2.112		2.029	2.181
H1n–H3b	1.695	2.294	1.657	2.230
H2n–H1b	2.335		2.248	
H2n–H2b	1.922		1.887	2.303
H2n–H3b	2.039		1.995	2.371
H3n–H1b	1.845	1.937	1.763	1.903
H3n–H2b	1.992		1.913	
H3n–H3b	2.279		2.191	

Hxn–Hxb	HPHT	
	4.0 GPa & 160 °C	
H1n–H1b	2.073	
H1n–H2b	2.307	
H2n–H1b	2.288	
H2n–H2b	1.956	2.194

ASSOCIATED CONTENT

Supporting Information Available:

Figure S1 shows the configuration of the DAC and the external heating system. **Figure S2** shows the 2D X-ray image of HPHT2 obtained at 17.5 GPa and 200°C. **Figure S3** shows the dihydrogen bonds that the H1n forms with adjacent molecules in the crystal structure of HPHT2 at 17.5 GPa and 200°C. **Figure S4** shows the optical micrograph of HPHT3 quenched to room temperature and decompressed to ~0.2 GPa. **Figure S5** shows the crystal structure of HP2 viewed in the *ab*-, *bc*-, and *ca*-planes. This information is available free of charge at the website: http://pubs.acs.org/

AUTHOR INFORMATION

Corresponding Author

Satoshi Nakano – *National Institute for Materials Science (NIMS), 1-1 Namiki, Tsukuba, Ibaraki 305-0044, Japan*; https://orcid.org/0000-0002-7010-9867; E-mail: nakano.satoshi@nims.go.jp

Authors

Hiroshi Fujihisa – *National Metrology Institute of Japan (NMIJ), National Institute of Advanced Industrial Science and Technology (AIST), Tsukuba Central 5, 1-1-1 Higashi, Tsukuba, Ibaraki 305-8565, Japan*; https://orcid.org/0000-0001-9308-153X

Hiroshi Yamawaki – *National Metrology Institute of Japan (NMIJ), National Institute of Advanced Industrial Science and Technology (AIST), Tsukuba Central 5, 1-1-1 Higashi, Tsukuba, Ibaraki 305-8565, Japan*; https://orcid.org/0000-0002-0145-9935

Takumi Kikegawa – *Photon Factory (PF), Institute of Materials Structure Science (IMSS), High Energy Accelerator Research Organization (KEK), 1-1 Oho, Tsukuba, Ibaraki 305-0801, Japan*

Author Contributions

The manuscript was written through contributions of all authors. All authors have given approval to the final version of the manuscript.

Notes

The authors declare no competing financial interest.

ACKNOWLEDGMENT

The authors are very grateful to Mr. Y. Masuda and Mr. T. Ikeda (NIMS) for their assistance with the machining process. We also thank Mr. K. Watanabe (Mitsubishi Electric System & Service Co., Ltd.) for supporting this work by maintaining the equipment in the synchrotron radiation X-ray beamline at PF. This work was partially supported by MEXT/JSPS KAKENHI (grant numbers JP18K05284 and JP21H00030) and the Tokodai Institute for Elemental Strategy (TIES) under the MEXT Element Strategy Initiative to Form Core Research Center, Japan (grant number JPMXP0112101001). Synchrotron radiation X-ray diffraction experiments were performed at BL-18C of KEK-PF under the approval of proposal numbers 2011G584, 2013G684, and 2015G565.

REFERENCES

(1) Demirci, U. B. Ammonia Borane, a Material with Exceptional Properties for Chemical Hydrogen Storage *Int. J. Hydrogen Energy* **2017**, *42* (15), 9978–10013, DOI: 10.1016/j.ijhydene.2017.01.154

(2) Staubitz, A.; Robertson, A. P. M.; Manners, I. Ammonia-Borane and Related Compounds as Dihydrogen Sources *Chem. Rev.* **2010**, *110* (7), 4079−4124, DOI: 10.1021/cr100088b

(3) Richardson, T.; de Gala, S.; Crabtree, R. H.; Siegbahn, P. E. M. Unconventional Hydrogen Bonds: Intermolecular B−H…H−N Interactions *J. Am. Chem. Soc.* **1995**, *117* (51), 12875−12876, DOI: 10.1021/ja00156a032

(4) Fukutani, K.; Yoshinobu, J.; Yamauchi, M.; Shima T.; Orimo, S. Hydrogenomics: Efficient and Selective Hydrogenation of Stable Molecules Utilizing Three Aspects of Hydrogen *Catalysis Lett.* **2022**, *152*, 1583–1597, DOI: 10.1007/s10562-021-03750-1

(5) Epstein, L. M.; Shubina, E. S. New Types of Hydrogen Bonding in Organometallic Chemistry *Coord. Chem. Rev.* **2002**, *231* (1−2), 165−181, DOI: 10.1016/S0010-8545(02)00118-2

(6) Drozdov, A. P.; Kong, P. P.; Minkov, V. S.; Besedin, S. P.; Kuzovnikov, M. A.; Mozaffari, S.; Balicas, L.; Balakirev, F. F.; Graf, D. E.; Prakapenka, V. B.; Greenberg, E.; Knyazev, D. A.; Tkacz M.; Eremets, M. I. Superconductivity at 250 K in Lanthanum Hydride under High Pressures *Nature* **2019**, *569*, 528–531, DOI: 10.1038/s41586-019-1201-8

(7) Somayazulu, M.; Ahart, M.; Mishra, A. K.; Geballe, Z. M.; Baldini, M.; Meng, Y.; Struzhkin, V. V.; Hemley, R. J. Evidence for Superconductivity above 260 K in Lanthanum Superhydride at Megabar Pressures *Phys. Rev. Lett.* **2019**, *122* (2), 027001-1–6, DOI: 10.1103/PhysRevLett.122.027001

(8) Frueh, S.; Kellett, R.; Mallery, C.; Molter, T.; Willis, W. S.; King'ondu, C.; Suib, S. L. Pyrolytic Decomposition of Ammonia Borane to Boron Nitride *Inorg. Chem.* **2011**, *50* (3), 783–792, DOI: 10.1021/ic101020k

(9) Sun, Y.; Chen, J.; Drozd, V.; Durigin, A.; Najiba, S.; Liu, X. Phase Boundary of Pressure-Induced *I*4*mm* to *Cmc*2_1 Transition in Ammonia Borane at Elevated Temperature Determined using Raman Spectroscopy *Int. J. Hydrog. Energy* **2014**, *39* (16), 8293–8302, DOI: 10.1016/j.ijhydene.2014.03.070

(10) Sun, Y.; Chen, J.; Drozd, V.; Najiba, S.; Bollinger, C. Behavior of Decomposed Ammonia Borane at High Pressure *J. Phys. Chem. Solids* **2015**, *84*, 75–79, DOI: 10.1016/j.jpcs.2014.12.004

(11) Huang, Y.; Huang, X.; Zhao, Z.; Li, W.; Jiang, S.; Duan, D.; Bao, K.; Zhou, Q.; Liu, B.; Cui, T. Experimental Verification of the High Pressure Crystal Structures in NH_3BH_3 *J. Chem. Phys.* **2014**, *140* (24), 244507-1−9, DOI: 10.1063/1.4884819

(12) Nakano, S.; Sano-Furukawa, A.; Hattori, T.; Machida, S.; Komatsu, K.; Fujihisa, H.; Yamawaki, H.; Gotoh, Y.; Kikegawa, T. Observation of Dihydrogen Bonds in High-Pressure Phases of Ammonia Borane by X-ray and Neutron Diffraction Measurements *Inorg. Chem.* **2021**, *60* (5), 3065–3073, DOI: 10.1021/acs.inorgchem.0c03345

(13) Nakano, S.; Fujihisa, H.; Yamawaki, H.; Kikegawa, T. Influence of Pressure-Induced Formation of Dihydrogen Bonds on Lattice Parameters, Volume, and Vibrational Modes of Ammonia Borane *J. Chem. Phys.* **2022**, *157* (23), 234702–1 ~ –10, DOI: 10.1063/5.0128003

(14) Nylén, J.; Sato, T.; Soignard, E.; Yarger, J. L.; Stoyanov, E.; Häussermann, U. Thermal Decomposition of Ammonia Borane at High Pressures *J. Chem. Phys.* **2009**, *131* (10), 104506-1−7, DOI: 10.1063/1.3230973

(15) Nylén, J.; Eriksson, L.; Benson, D.; Häussermann, U. Characterization of a High Pressure, High Temperature Modification of Ammonia Borane (BH_3NH_3) *J. Chem. Phys.* **2013**, *139* (5), 054507-1−7, DOI: 10.1063/1.4817188

(16) Wang, L.; Duan, D.; Zhao, B.; Bao, K.; Yu, H. Structural and Dynamic Properties of the High-Pressure, High-Temperature Phase of Solid Ammonia Borane *J. Phys. Chem. C* **2019**, *123* (11), 6326−6332, DOI: 10.1021/acs.jpcc.8b10403

(17) Chen, J.; Drozd, V.; Sun, Y.; Najiba, S. Ammonia Borane at High Pressures *Chin. Sci. Bull.* **2014**, 59, 5227–5234, DOI: 10.1007/s11434-014-0619-5

(18) Lin, Y.; Mao, W. L. High-Pressure Storage of Hydrogen Fuel: Ammonia Borane and its Related Compounds *Chin. Sci. Bull.* **2014**, *59*, 5235−5240, DOI: 10.1007/s11434-014-0624-8

(19) Takemura, K.; Sahu, P. C.; Kunii, Y.; Toma, Y. Versatile Gas-Loading System for Diamond-Anvil Cells *Rev. Sci. Instru.* **2001**, *72* (10), 3873−3876, DOI: 10.1063/1.1396667

(20) Yamaoka, S.; Shimomura, O.; Fukunaga, O. Simultaneous Measurements of Temperature and Pressure by the Ruby Fluorescence Line *Proc. Japan Acad., Ser. B*, **1980**, *56* (3), 103−107, DOI: 10.2183/pjab.56.103

(21) Ragan, D. D.; Gustavsen, R.; Schiferl, D. Calibration of the Ruby R1 and R2 Fluorescence Shifts as a Function of Temperature from 0 to 600 K *J. Appl. Phys.* **1992**, *72* (12), 5539, DOI: 10.1063/1.351951

(22) Mao, H. K.; Xu, J.; Bell, P. M. Calibration of the Ruby Pressure Gauge to 800 kbar under Quasi-Hydrostatic Conditions *J. Geophys. Res.* **1986**, *91* (B5), 4673–4676, DOI: 10.1029/JB091iB05p04673

(23) Zha, C.-S.; Mao, H.-K.; Hemley, R. J. Elasticity of MgO and a Primary Pressure Scale to 55 GPa *PNAS* **2000**, *97* (25), 13494–13499, DOI: 10.1073/pnas.240466697

(24) Lin, F.; Levitas, V. I.; Pandey, K. K.; Yesudhas, S.; Park, C. In-situ study of rules of nanostructure evolution, severe plastic deformations, and friction under high pressure *Mater. Res. Lett.* **2023**, *11* (9), 757–763, DOI: 10.1080/21663831.2023.2231983

(25) Seto, Y.; Hamane, D.; Nagai, T.; Fujino, K. Fate of Carbonates within Oceanic Plates Subducted to the Lower Mantle, and a Possible Mechanism of Diamond Formation *Phys. Chem. Minerals* **2008**, *35*, 223−229, DOI: 10.1007/s00269-008-0215-9

(26) Dassault Systèmes Americas Corp. *BIOVIA Materials Studio Reflex website*. https://www.3ds.com/fileadmin/PRODUCTS-SERVICES/BIOVIA/PDF/BIOVIA-material-studio-reflex.pdf (accessed 2023-09-19).

(27) Dollase, W. A. Correction of Intensities for Preferred Orientation in Powder Diffractometry: Application of the March Model *J. Appl. Cryst.* **1986**, *19* (4), 267 − 272, DOI: 10.1107/S0021889886089458

(28) Clark, S. J.; Segall, M. D.; Pickard, C. J.; Hasnip, P. J.; Probert, M. I. J.; Refson, K.; Payne, M. C. First Principles Methods using CASTEP *Z. Kristallogr.* **2005**, *220* (5–6), 567−570, DOI: 10.1524/zkri.220.5.567.65075

(29) Perdew, J. P.; Ruzsinszky, A.; Csonka, G. I.; Vydrov, O. A.; Scuseria, G. E.; Constantin, L. A.; Zhou, X.; Burke, K. Restoring the Density-Gradient Expansion for Exchange in Solids and Surfaces *Phys. Rev. Lett.* **2008**, *100* (13), 136406-1–4, DOI: 10.1103/PhysRevLett.100.136406

(30) Vanderbilt, D. Soft Self-Consistent Pseudopotentials in a Generalized Eigenvalue Formalism *Phys. Rev. B* **1990**, *41* (11), 7892−7895, DOI: 10.1103/PhysRevB.41.7892

(31) Monkhorst, H. J.; Pack, J. D. Special Points for Brillouin-Zone Integrations *Phys. Rev. B* **1976**, *13* (12), 5188−5192, DOI: 10.1103/PhysRevB.13.5188

(32) Bowden, M.; Autrey, T.; Brown, I.; Ryan, M. The Thermal Decomposition of Ammonia Borane: A Potential Hydrogen Storage Material *Current Appl. Phys.* **2008**, *8* (3–4), 498–500, DOI: 10.1016/j.cap.2007.10.045

(33) Liang, Y.; Tse, J. S. First-Principles Study on the Mechanisms for H_2 Formation in Ammonia Borane at Ambient and High Pressure *J. Phys. Chem. C* **2012**, *116* (3), 2146–2152, DOI: 10.1021/jp206161m